RSC Advances

PAPER

Published on 03 July 2026


Cite this: DOI: 10.1039/d6ra03318k

# Sustainable electrocatalysis: overcoming signal convolution of dopamine and paracetamol at a pristine graphene interface

Lê Thi Kim Dung, [a] Do Mai Nguyen, [b] Nguyen Truong Son, [a] Nguyen Minh Quang, [c] Dinh Tuan, [d] Tran Thanh Tam Toan *[e] and Vo Chau Ngoc Anh *[a]

Received 18th April 2026
Accepted 18th May 2026

DOI: 10.1039/d6ra03318k

rsc.li/rsc-advances

Simultaneous electrochemical quantification of dopamine and paracetamol is often hindered by overlapping oxidation potentials and severe surface passivation. To address this analytical gap, a completely reagent-free fabrication approach was developed to construct an electrochemically reduced graphene oxide (ERGO) modified glassy carbon electrode (GCE). The reliance on toxic reducing agents was entirely eliminated by utilizing a direct cathodic potential scan. Through this green process, the conductive carbon network was restored, yielding a highly active electrocatalytic interface. Complete baseline separation between the two target analytes was successfully achieved. Under optimized acidic conditions at pH 3.0, a broad linear dynamic range from 0.1 to 20 μM was obtained for both compounds. Furthermore, the limits of detection (LOD) were 0.008 μM for dopamine (DOP) and 0.016 μM for paracetamol (PAR). Excellent target selectivity was demonstrated even when the sensor was challenged with highly concentrated biological interferents such as ascorbic acid and uric acid. Finally, the platform's practical reliability was validated by analysing commercial pharmaceutical formulations, yielding recovery rates of 96.1–104.1%. These findings were statistically equivalent to standard chromatographic measurements, confirming that a highly accurate, eco-friendly tool is provided for routine clinical monitoring.

## Introduction

Maintaining the delicate homeostasis of neurotransmitters is a fundamental prerequisite for human physiological stability.[1] Dopamine (DOP) is a central catecholamine neurotransmitter that governs crucial nervous system functions, including motor control, emotion regulation, and cognition.[2,3] Aberrant fluctuations in DOP levels frequently serve as early biomarkers for severe neurological pathologies, including Parkinson's disease, schizophrenia, and depression.[4–8] Alongside clinical diagnostics, paracetamol (PAR) is globally recognized as one of the most heavily consumed analgesic and antipyretic medications.[9,10] While exceptionally safe at therapeutic dosages, excessive ingestion leads to the accumulation of toxic metabolites that induce severe hepatotoxicity and nephrotoxicity.[9] Recent pharmacological evidence indicates that elevated PAR concentrations significantly affect the extent of DOP-related neurodegeneration.[10] Consequently, the simultaneous and precise quantification of DOP and PAR transcends routine pharmaceutical quality control to become an urgent clinical imperative for disease monitoring and toxicological assessment.

Traditionally, the quantification of these pharmaceutical compounds relies heavily on highly accurate techniques such as high-performance liquid chromatography (HPLC)[11] and spectrophotometry.[12] These methodologies are inherently constrained by bulky instrumentation, expensive operational costs, and the inability to execute real-time screening. Electrochemical sensing technology offers a highly elegant alternative, providing rapid response times, remarkable sensitivity, and point-of-care adaptability.[13] Despite these advantages, a profound analytical bottleneck has stalled progress in this domain. The overlapping oxidation potentials of DOP and PAR on conventional unmodified carbon electrodes inevitably lead to severe signal convolution and mutual interference.[14,15] Compounding this challenge is the issue of electrode fouling.[14,15] The electrochemical oxidation of these molecules generates highly reactive byproducts that rapidly adsorb and passivate the electrode surface. This rapid contamination

[a]University of Medicine and Pharmacy, Hue University, 530000, Vietnam. E-mail: vcnanh@hueuni.edu.vn

[b]University of Science and Education, Danang University, Danang City, 550000, Vietnam

[c]Faculty of Chemical Engineering, Industrial University of Ho Chi Minh City, Ho Chi Minh City, 700000, Vietnam

[d]Faculty of Pharmacy, Nam Can Tho University, 168 Nguyen Van Cu Street, An Binh Ward, Can Tho City, Vietnam

[e]Phu Xuan University, Hue City, 530000, Vietnam. E-mail: toan.tran@pxu.edu.vn

drastically compromises the long-term stability, reproducibility, and sensitivity of conventional sensing platforms.[16–18]

To engineer an interface capable of decoupling these convoluted signals, various sophisticated architectures, including metal oxide composites, conducting polymers, and bimetallic nanoparticles, have been extensively explored.[19,20] While effective, these functionalization strategies frequently require tedious multistep fabrication protocols, expensive reagents, and suffer from poor batch-to-batch reproducibility.[14,15] Among the diverse nanomaterials, two-dimensional reduced graphene oxide (rGO) has emerged as a superior standalone scaffold.[21] It significantly accelerates interfacial electron transfer and provides an expansive network for aromatic stacking interactions.[22,23] Nevertheless, the traditional synthesis of this material presents a critical flaw. Chemical reduction routes heavily depend on highly toxic and environmentally hazardous agents such as hydrazine or sodium borohydride.[24] These aggressive protocols pose severe ecological threats and inherently leave residual chemical impurities on the carbon scaffold. Such contaminants can poison the electrocatalytic interface, hinder electron mobility, and ultimately restrict the material anti fouling capabilities and overall analytical performance.[22,23]

Despite the sheer volume of literature on graphene-based sensors, establishing a truly sustainable, anti-fouling platform for the definitive baseline resolution of DOP and PAR remains a conspicuous research gap. Specifically, the strategic exploitation of electrochemically reduced graphene oxide (ERGO) to systematically overcome both the overpotential and fouling issues in DOP and PAR mixtures has been vastly underexplored.[25–30] The ERGO synthesis represents a paradigm shift in green chemistry by utilizing electrons as the sole reducing agent within an aqueous electrolyte, thereby entirely circumventing the need for hazardous chemical reductants.[31–38] This direct electrodeposition process enables precise control over the degree of reduction, elegantly restoring the $sp^2$ graphitic network while forming a pristine, defect-rich electrocatalytic interface.[39,40] The uniquely tailored surface chemistry of ERGO facilitates rapid electron kinetics and preferential analyte adsorption, both of which are critical for mitigating passivation effects.[41–43]

Addressing this critical void, the present study introduces a facile, fully reagent-free fabrication method for an ERGO-modified glassy carbon electrode (ERGO/GCE) that decisively revitalizes the simultaneous electroanalysis of DOP and PAR. This meticulously engineered, eco-friendly heterointerface drastically lowers the activation overpotential, resulting in an unprecedented baseline separation between the oxidation peaks of the two analytes. Furthermore, the pristine nature of the ERGO film confers exceptional resistance against the accumulation of pharmaceutical oxidation byproducts. By simultaneously solving the ecological pitfalls of material synthesis and the analytical hurdles of signal overlap and surface passivation, this work delivers an ultra-sensitive and robust tool for modern pharmaceutical monitoring. The exceptional analytical performance achieved herein underscores the vast potential of green electroanalysis in advancing clinical and environmental diagnostics.

# Experimental

## Chemicals

Reagents of the highest analytical purity were acquired and applied directly without any subsequent refinement. The essential chemical inventory, encompassing dopamine, paracetamol, graphene oxide, ascorbic acid, uric acid, hypoxanthine, clenbuterol, ammonium sulfate, sodium chloride, iron chloride, and calcium nitrate, was obtained from standard suppliers and used throughout the voltammetric investigations. To establish the supporting electrolyte, monosodium phosphate and disodium phosphate were mixed to formulate phosphate buffer solutions spanning a pH range from 2.0 to 6.0. The specific acidity levels in these environments were strictly controlled by carefully adjusting the molar proportions of the two phosphate salts. Pure distilled water was exclusively selected to prepare all aqueous media demanded by the experimental protocol. The exact pH conditions required for the concurrent electroanalytical tracking of dopamine and paracetamol at the surface of the modified glassy carbon electrodes were guaranteed by this rigorous preparation procedure.

Solutions of 0.20 M phosphate (PBS) buffer were formulated by mixing $NaH_2PO_4$ and $Na_2HPO_4$ to regulate the acidity levels between pH 2.0 and 6.0.

## Instruments

The chemical functional groups were analyzed by Fourier transform infrared (FTIR) spectroscopy using a Shimadzu IR Prestige-21 spectrometer manufactured in Japan. For the acquisition of Raman scattering data, an XPLORA apparatus from HORIBA was utilized. Furthermore, crystallographic properties were evaluated by X-ray diffraction (XRD) on a German Bruker D8 Advance diffractometer, operated with a Cu $K_\alpha$ radiation source ($\lambda = 0.1514$ nm) and a 532 nm laser.

All voltammetric measurements were performed on a Corrtest machine. A glassy carbon electrode (GCE) with a geometric diameter of 2.8 mm was used as the working electrode. Furthermore, the standard three-electrode system was completed with a platinum wire counter electrode and an Ag/AgCl reference half-cell immersed in a saturated KCl solution.

## The fabrication of ERGO/GCE

The modified electrode was prepared by direct electrochemical reduction. Initially, the GCE surface was polished with an alumina slurry, then rinsed with ethanol and distilled water. After the cleaning step, a specific volume of the precursor suspension, containing 5 μg of GO, was cast onto the carbon surface. The electrode was then dried at room temperature.

The electrochemical conversion of GO to rGO was performed using CV. The modified electrode was immersed in a 0.1 M PBS buffer solution at pH 3.0. The reduction process was performed in a potential range from 0 V to −1.5 V (*vs.* Ag/AgCl) at a scan rate of 0.1 V $s^{-1}$. While up to 15 continuous potentiodynamic cycles were initially investigated to comprehensively study the *in*

*situ* reduction behavior and structural conversion of the film, exactly 9 cycles were ultimately selected for the routine fabrication of all working electrodes used in subsequent quantitative analyses. Through this optimized procedure, the oxygen-containing functional groups were efficiently removed from the carbon structure by the applied electrical potential. Consequently, the material's electrical conductivity was restored. The use of chemical reducing agents was completely avoided, thereby preventing the accumulation of toxic residues on the electrode surface.

### The preparation of the real samples

To accurately evaluate the practical applicability of the developed sensing platform, six distinct commercial pharmaceutical products were procured from a local pharmacy in Hue city, Vietnam. These commercial formulations were categorized into solid dosage forms containing paracetamol and liquid injectable solutions containing dopamine.

For the solid pharmaceutical preparations, including Panadol Extra, Efferalgan, and Hapacol 150, a rigorous homogenization protocol was followed. Initially, twenty individual tablets or powder packets from each specific brand were randomly selected. Their total mass was precisely measured to determine the average weight per unit. Subsequently, these solid samples were thoroughly pulverized and ground into a completely homogeneous powder utilizing an agate mortar. An exact portion of this finely ground powder was carefully weighed and completely dissolved in warm distilled water. To eliminate any insoluble formulation excipients and binder materials, the resulting aqueous suspension was filtered through a 0.45 μm microporous membrane. The clear filtrate was finally transferred into a calibrated volumetric flask and diluted to the predetermined mark with pure distilled water to establish the primary stock solution.

Conversely, a simplified dilution procedure was applied to the liquid pharmaceutical formulations, including Dopamin Giulini, Limdopa Inj 200 mg, and Dopamin Rotexmedica. A highly precise volume of the active liquid was directly extracted from the commercial ampoules utilizing a volumetric pipette. This extracted analytical liquid was immediately transferred to a separate volumetric flask and diluted to the desired concentration with distilled water to prepare the target test solutions.

For the ultimate voltammetric quantification step, specific aliquots derived from these prepared pharmaceutical stocks were strategically introduced into the electrochemical cell. The measurement vessel was prefilled with the optimized 0.1 M PBS buffer solution maintained strictly at pH 3.0. The standard addition methodology was exclusively employed during the DPV measurements to accurately quantify the target analytes and to effectively neutralize any potential matrix interference effects.

## Results and discussions

### Characterization

The structural and chemical transformations accompanying the electrochemical reduction of graphene oxide were systematically elucidated using a combination of spectroscopic and crystallographic techniques, as presented in Fig. 1.

Infrared spectroscopy provided compelling evidence regarding the elimination of oxygenated moieties as depicted in Fig. 1a. The precursor material displayed prominent absorption bands corresponding to various oxygen-containing functional groups. Specifically, the broad transmission signal near 3400 $cm^{-1}$ signifies the stretching vibrations of hydroxyl entities, whereas the distinct peak around 1720 $cm^{-1}$ corresponds to the carbonyl stretching. Following the applied cathodic potential scanning, the spectrum of the electrochemically reduced graphene oxide revealed a drastic attenuation of these characteristic signals. This profound diminution corroborates the successful expulsion of labile oxygen-containing groups and the concurrent reconstitution of the electrically conductive carbon framework.

Further structural insights were obtained from Raman spectroscopy, as shown in Fig. 1b. Both materials exhibited the quintessential D band near 1350 $cm^{-1}$, representing lattice defects and the G band near 1580 $cm^{-1}$ associated with the in-plane vibrations of $sp^2$ hybridized carbon atoms. These deliberately introduced topological imperfections are highly advantageous, as they provide a vast array of active centres that facilitate accelerated charge-transfer kinetics in sensing applications.

Finally, X-ray diffraction (XRD) was used to monitor changes in the interlamellar spacing, as shown in Fig. 1c. The oxidized precursor exhibited a sharp diffraction peak at approximately 10.6°, a hallmark of an expanded interlayer distance resulting from the intercalation of water molecules and bulky oxygen functionalities. Upon electrochemical reduction, this pronounced peak completely disappeared. In its place, as explicitly illustrated in the magnified inset of Fig. 1c, a broad diffraction pattern emerged around 24.5°, representing the characteristic (002) crystallographic plane of graphitic structures. The distinctly broad and relatively low-intensity nature of this peak confirms the formation of a few-layer, short-range-ordered macroscopic architecture, a fundamental crystallographic characteristic of restacked electrochemically reduced graphene sheets. This definitive shift confirms the successful ejection of the intercalated functional groups and the subsequent restacking of the two-dimensional carbon sheets, thereby validating the phase transformation from the insulating precursor to the highly conductive electrocatalytic scaffold.

## The electrochemically simultaneous detection of DOP and PAR using ERGO/GCE electrode modification

### The electrode behavior

To evaluate the performance of the modified electrode, the electrochemical behavior of a mixture containing 10 μM DOP and 10 μM PAR was tested. As shown in Fig. 2a, CV was performed in 0.1 M PBS buffer at pH 3.0 with a scan rate of 0.2 V $s^{-1}$ and a potential scan range from −0.2 V to +1.0 V (*vs.* Ag/AgCl).

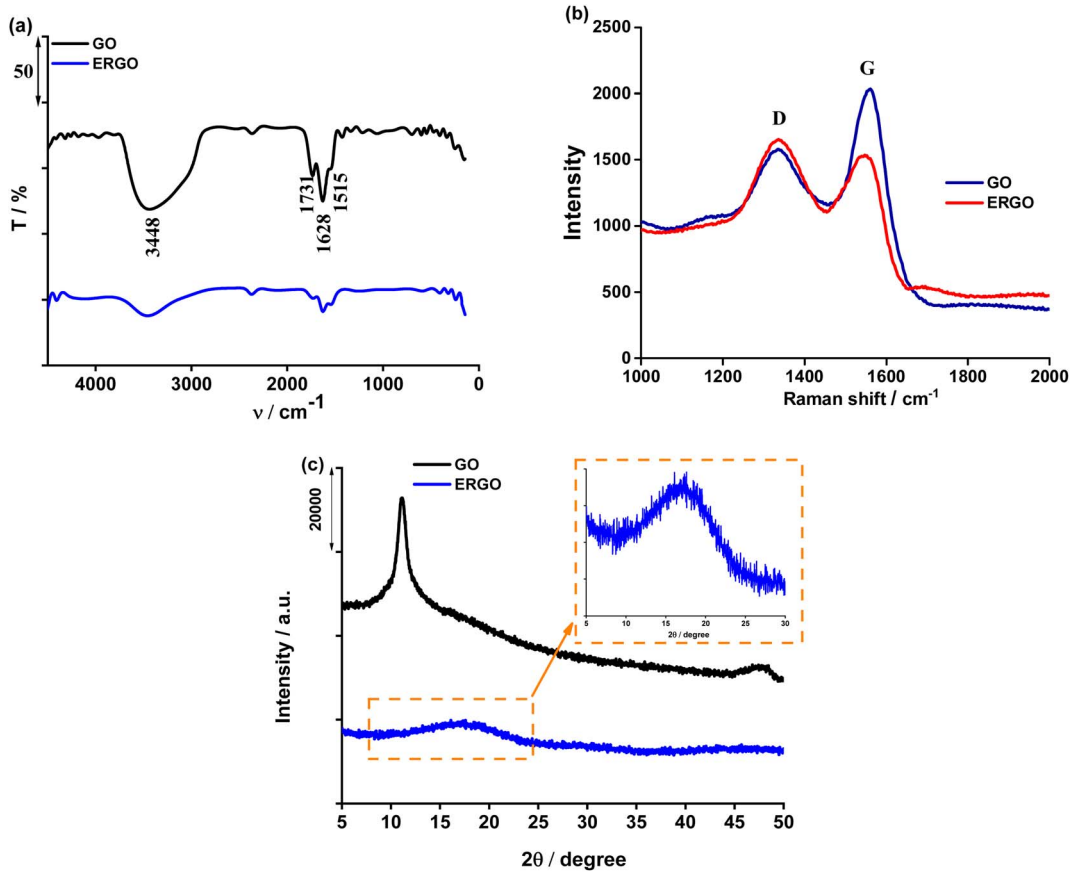


Fig. 1 (a) FTIR spectra, (b) Raman spectra, and (c) XRD patterns of GO and ERGO.

Comparing the curves reveals a clear difference in catalytic activity among the electrode surfaces.

On the bare GCE, the oxidation signals for both DOP and PAR were very weak. The two peaks merged into a single broad wave. This overlap occurs because the bare electrode exhibits slow electron-transfer kinetics and cannot resolve the closely spaced oxidation potentials of these two molecules. Therefore, the bare electrode lacks the sensitivity and selectivity needed to distinguish them.

A major improvement was observed when using the electrode modified with ERGO. When testing the DOP and PAR mixture with this ERGO-modified electrode, the peak currents increased significantly. More importantly, the ERGO layer reduced the activation overpotential. This caused the oxidation potential of DOP to shift to a more negative value, while PAR shifted to a more positive value. As a result, the previously merged signal split into two sharp and independent peaks.

Test conditions: potential scan range −0.2 V–+1.0 V (*vs.* Ag/AgCl), 10 μM DOP and 10 μM PAR in buffer solution PBS 0.1 M (pH = 3.0), scan rate: 0.2 V $s^{-1}$.

This excellent separation is due to the unique structure of the ERGO film. The electrical reduction removes insulating oxygen groups, which restores the conductive carbon network for fast electron transfer. At the same time, the remaining surface defects act as highly active catalytic centres. Furthermore, the flat graphene structure forms strong interactions with the aromatic rings of DOP and PAR. These interactions help target molecules bind directly to the electrode surface, greatly boosting signal intensity.

Comparing the curves in Fig. 2 clearly shows that the ERGO modified electrode provides the best performance. It effectively increases sensitivity and completely eliminates signal overlap. Because of the perfect peak separation and high current response, the ERGO-modified electrode was chosen as the optimal platform for all subsequent optimisation and quantitative experiments.

The profound correlation between the material fabrication process and the resulting electrocatalytic performance is elegantly demonstrated through the integrated analysis of Fig. 2b and c. This logical progression provides the fundamental evidence for the superior sensitivity of the ERGO interface.

The *in situ* evolution of the catalytic film is explicitly monitored in Fig. 2b. During the initial scan cycle, a strong irreversible reduction peak emerges at approximately −1.2 V. This indicates the rapid removal of oxygen-containing functional groups, such as hydroxyl and epoxy moieties, which otherwise hinder conductivity on the graphene oxide lattice. As the scan cycles progress through the 4th and 5th cycles toward the 9th and 10th cycles, the intensity of this reduction signal diminishes significantly and reaches a steady state. This attenuation confirms the nearly complete restoration of the conductive $sp^2$

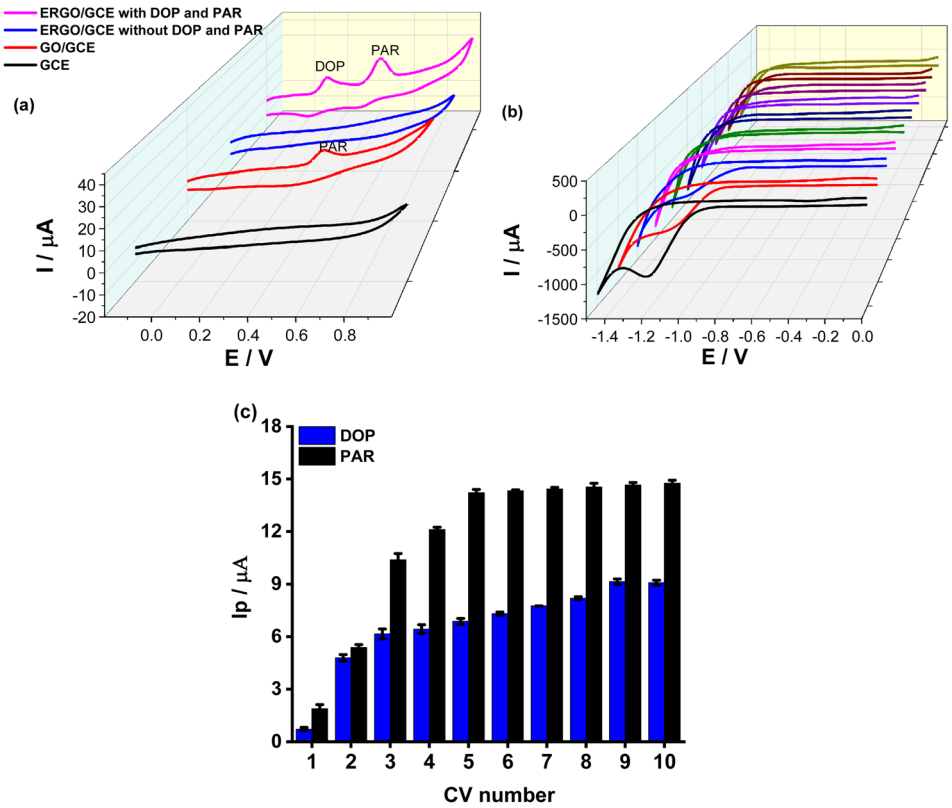


Fig. 2 (a) The CVs of DOP and PAR at various electrodes, (b) the CV curves of reduction of GO to rGO over 10 scan cycles, (c) the dependence of the anodic peak currents of DOP and PAR on the number of scan cycles.

graphitic network and the creation of a pristine, defect-rich surface that serves as a highly active platform for continuous electron transfer.

This structural transformation directly drives the analytical performance illustrated in Fig. 2c. As the insulating oxygen groups are progressively removed during consecutive scans, the anodic peak currents for both DOP and PAR exhibit a substantial, steady rise from the 1st to the 10th scan cycle. This enhancement demonstrates that the actively forming film provides a vastly expanded effective surface area and abundant active sites for analyte adsorption. Interestingly, by the 10th scan cycle, the recorded peak currents are identical to those at the 9th cycle, indicating that the electrocatalytic interface has reached its maximum active capacity. Therefore, to deliberately minimise fabrication time while ensuring optimal signal intensity, nine scan cycles were selected as the optimal parameter for all subsequent analytical studies.

The rationality of this fabrication strategy is ultimately validated by the comparative data presented in Fig. 2a. While the initial, unmodified or GO-modified electrodes, which lack sufficient conductivity, exhibit only faint, ill-defined signals for the analytes, the ERGO-modified electrode synthesised after optimal 9 cycles displays a remarkable transformation. It successfully resolves the previously merged signals into two sharp, independent, and high-intensity peaks for both target molecules. This definitive baseline separation conclusively demonstrates that the engineered electrochemical reduction process yielded a highly active and selective sensing platform, fully ready for simultaneous quantitative tracking.

## Impact of pH

To optimize the performance of the sensing platform and to elucidate the reaction kinetics, the influence of hydrogen ion concentration on the electrochemical behavior of DOP and PAR was systematically investigated. This process involved carefully analyzing three distinct aspects of the data presented in Fig. 3.

The first observation is depicted in Fig. 3a, which presents the cyclic voltammetry curves of a mixture containing 10 μM DOP and 10 μM PAR across various buffer solutions with changing pH values. The analysis of these curves reveals that as the pH of the solution increased, the oxidation peak potentials for both analytes shifted linearly towards more negative values. This distinct morphological shift provides clear evidence that protons directly participate in the electrochemical oxidation reaction at the interface between the ERGO-modified electrode and the solution.

In addition to the potential shift, the variation in peak current intensity with pH was carefully evaluated to determine the optimal operating conditions for the sensor, as shown in Fig. 3b. The catalytic current shows a strong dependence on the solution's pH. The plotted data reveal that the oxidation current signal reaches its maximum value at pH 3. This enhancement in current intensity in an acidic environment can be fundamentally explained by considering the acid dissociation constants

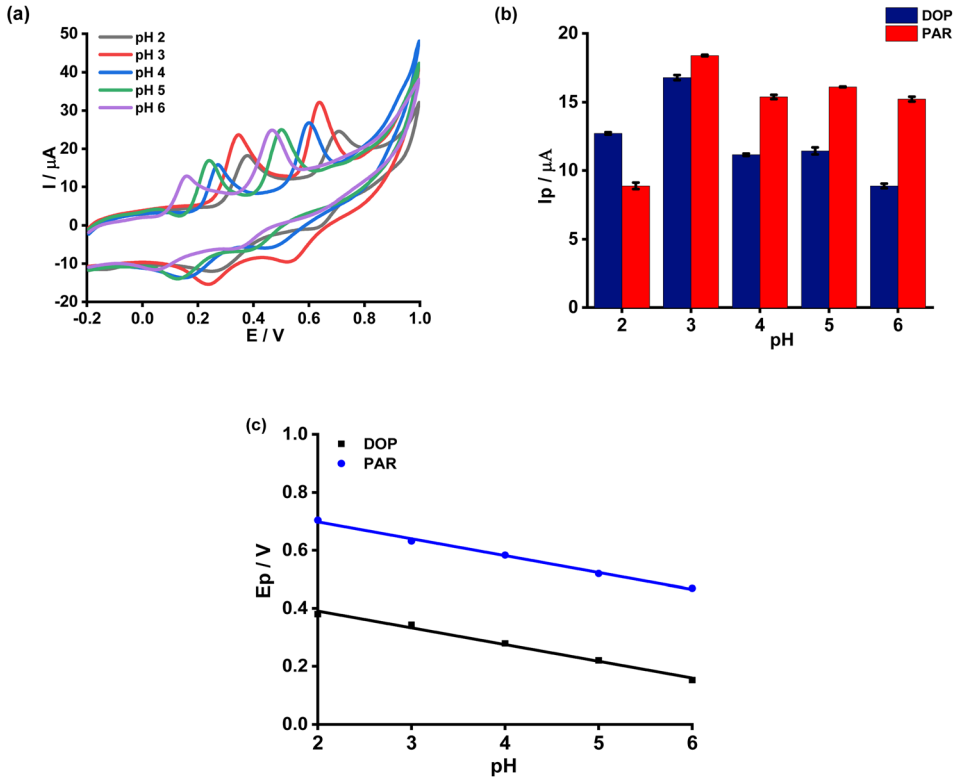


Fig. 3 (a) The CV curves of the DOP and PAR mixture in 0.1 M PBS buffer solutions with varying pH values (from 2.0 to 6.0), (b) the dependence of the anodic peak currents on the varying pH values, and (c) the linear relationship between the anodic peak potentials ($E_p$) and pH. Test conditions: potential scan range −0.2 V–+1.0 V (*vs.* Ag/AgCl), 10 μM DOP and 10 μM PAR in buffer solution PBS 0.1 M (pH = 3.0), scan rate: 0.2 V $s^{-1}$.

(pKa) of the target molecules. Based on the clear experimental results shown in Fig. 3b, the buffer solution at pH 3.0 was selected as the standard analytical environment for all subsequent simultaneous quantitative experiments. This strategic selection ensures that the sensing platform achieves the highest possible sensitivity and complete baseline separation. Crucially, from a practical standpoint, this specific acidic environment closely matches the chemical conditions of commercial dopamine hydrochloride injections. In industry, these pharmaceutical formulations are strictly maintained at low pH (typically 2.5 to 5.0) to prevent spontaneous auto-oxidation and degradation of the catecholamine structure. Thus, this optimized pH condition not only provides maximal electroanalytical performance but also guarantees direct compatibility with the targeted pharmaceutical sample matrices.

The kinetic nature of this process is further reinforced by Fig. 3c, which shows a linear relationship between the peak potential and pH. Based on the experimental data, linear regression analysis between the peak potential and the pH generated the following mathematical equations:

$$E_{p.DOP} = (-0.058 \pm 0.003)\text{pH} + (0.506 \pm 0.013)\ R = 0.991 \quad (3.1)$$

$$E_{p.PAR} = (-0.058 \pm 0.002)\text{pH} + (0.815 \pm 0.009)\ R = 0.996 \quad (3.2)$$

The slope values obtained from these empirical equations are 0.058 V for both DOP and PAR. This potential decay matches the theoretical value of 0.059 V predicted by the standard thermodynamic Nernst equation. This strict correlation definitively confirms that the electrocatalytic process for both pharmaceutical molecules involves the transfer of equal numbers of protons and electrons.

## Impact of scan rates

To elucidate the electron transfer kinetics and the mass transport mechanisms of the target molecules at the electrode interface, the influence of the potential scan rate on the electrochemical behavior of DOP and PAR was systematically investigated. This kinetic study was meticulously divided into three analytical aspects, corresponding to the specific panels in Fig. 4.

Initially, Fig. 4a presents the CV curves of the binary mixture recorded at continuously increasing scan rates. A visual inspection of these voltammograms reveals a progressive increase in the anodic peak currents for both analytes as the scan rate increases. This dynamic current response indicates a highly active electrocatalytic surface capable of accommodating rapid charge exchanges.

To determine the predominant mass-transport regime, the relationship between the peak current and the square root of the scan rate was analyzed (Fig. 4b). The experimental data points exhibit an outstanding linear correlation:

$$I_{p,\ DOP} = (37.1 \pm 2.5)\nu^{1/2} + (0.7 \pm 1.2)\ R = 0.982 \quad (3.3)$$

$$I_{p,\ PAR} = (36.3 \pm 1.6)\nu^{1/2} + (3.7 \pm 0.8)\ R = 0.992 \quad (3.4)$$

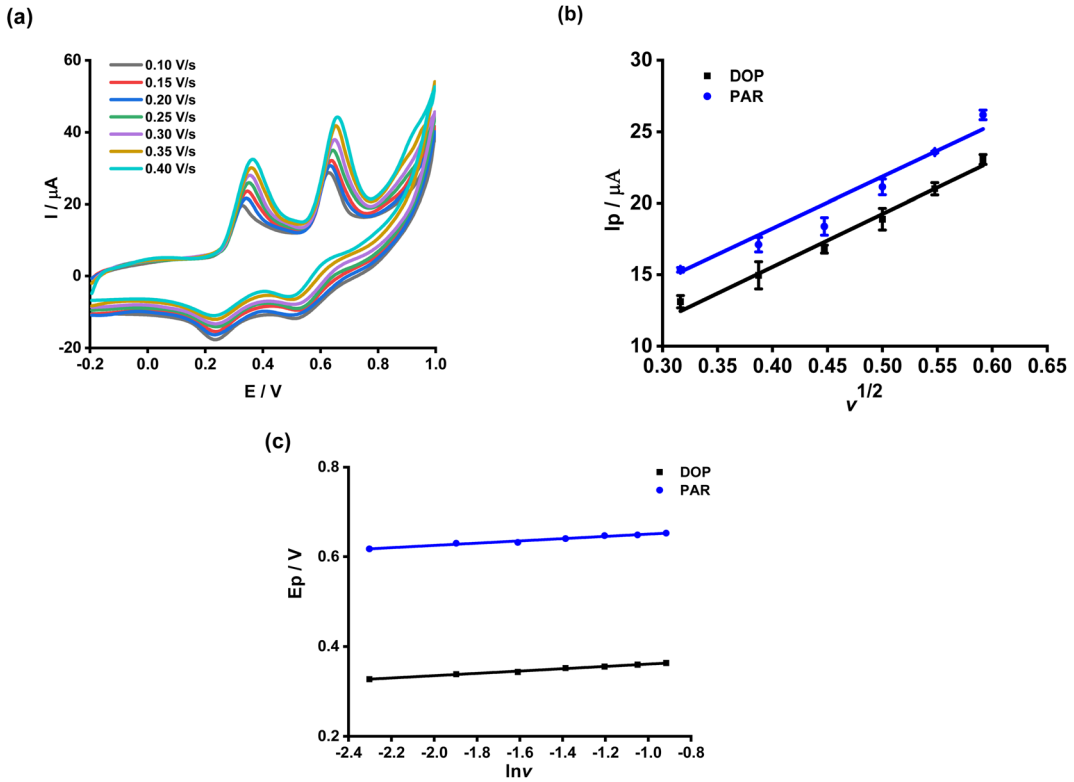


Fig. 4 (a) The CV curves of DOP and PAR at various scan rates, (b) the linear relationship between the anodic peak currents ($I_p$) and the square root of the scan rate ($\nu^{1/2}$), and (c) the linear relationship between the anodic peak potentials ($E_p$) and the natural logarithm of the scan rate (ln $\nu$). Test conditions: potential scan range −0.2 V–+1.0 V (*vs.* Ag/AgCl), 10 μM DOP and 10 μM PAR in buffer solution PBS 0.1 M (pH = 3.0), scan rate: 0.2 V $s^{-1}$.

Further kinetic insights were extracted by observing the oxidation peak potentials. As the scan rate increased, the peak potentials for both DOP and PAR shifted positively, confirming the irreversible nature of the electrochemical oxidation at the sensing interface. According to the Laviron theory for irreversible systems, the peak potential holds a linear relationship with the natural logarithm of the scan rate, which is clearly illustrated in Fig. 4c. The linear regression equations are formulated as:

$$E_{p,\ DOP} = (0.026 \pm 0.001)\ln \nu + (0.386 \pm 0.001)\ R = 0.995 \quad (3.5)$$

$$E_{p,\ PAR} = (0.025 \pm 0.002)\ln \nu + (0.676 \pm 0.002)\ R = 0.982 \quad (3.6)$$

Based on the theory proposed by Laviron,[44] the relation of $E_p$ *vs.* ln $\nu$ can be expressed as eqn (3.7) in an irreversible process:

$$E_p = E^0 - \frac{RT}{(1-\alpha)nF}\ln\frac{RTK_s}{(1-\alpha)nF} + \frac{RT}{(1-\alpha)nF}\ln \nu \quad (3.7)$$

where "$E^0$ = the formal redox potential, $T$ = 298 K, $R$ = 8.314 J mol $K^{-1}$, $\alpha$ = the charge transfer coefficient, $k_s$ = the heterogeneous electron transfer rate constant of the surface-confined redox couple, $n$ = the number of electrons transferred, $\nu$ = the scan rate (V $s^{-1}$), and $F$ = 96 480C $mol^{-1}$".

This means that the DOP and PAR oxidation reactions are attached to two electrons and two protons at the modified electrodes (Scheme 1). This critical finding perfectly complements the earlier pH study, thereby providing definitive proof that the electrocatalytic oxidation of DOP and PAR on the ERGO/GCE surface proceeds *via* a concerted mechanism involving the simultaneous exchange of two electrons and two protons to form their respective quinone products.[22,45] The electrochemical irreversibility was further substantiated by evaluating the peak potential separation ($\Delta E_p = E_{pa} - E_{pc}$). For a reversible two-electron process, a theoretical $\Delta E_p$ of approximately 29.5 mV (59/2 mV, with "2" is the number of transferred electrons) is expected at 25 °C, independent of the scan rate. However, in the recorded voltammograms (Fig. 2a), the cathodic peaks for both DOP and PAR were significantly attenuated or virtually absent, resulting in an abnormally large or undefined $\Delta E_p$. This phenomenon is a hallmark of an irreversible process in which the electrogenerated products are rapidly consumed by subsequent chemical pathways, such as intramolecular cyclization or hydrolysis, before cathodic reduction can occur. The significant deviation from the Nernstian $\Delta E_p$ requirement, coupled with the linear dependence of $E_p$ on ln $\nu$, definitively confirms that the oxidation of the target analytes at the ERGO interface is governed by irreversible kinetics.

## Linear range and limit of detection

### Increasing an analyte concentration in the absence of another analyte concentration

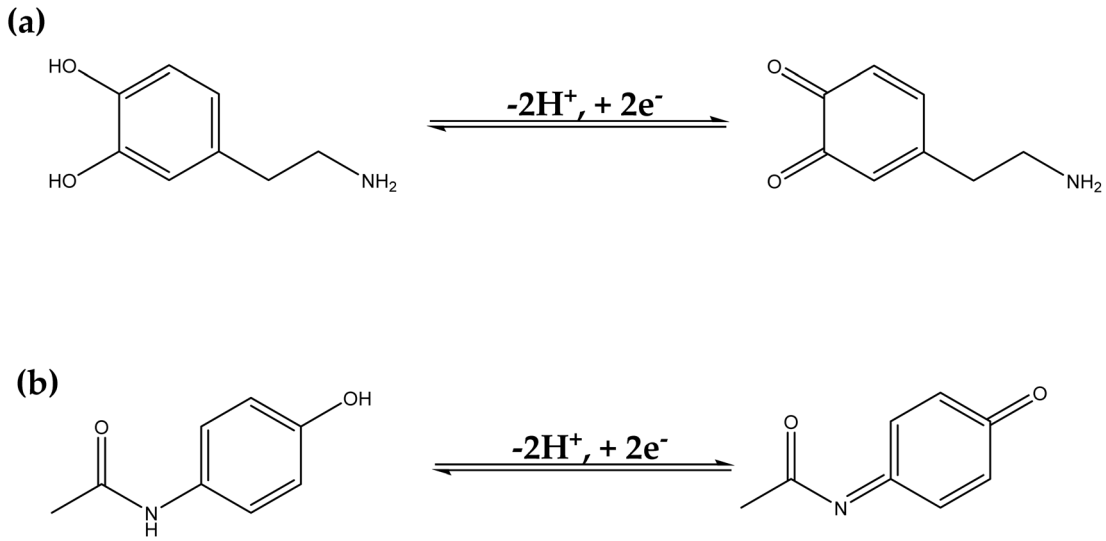


Scheme 1 The suggested oxidation mechanism of (a) DOP and (b) PAR.[22,45]

*For DOP individual detection.* To evaluate the quantitative capability of the modified electrode for individual analytes, DPV was employed due to its superior sensitivity. Fig. 5 presents the individual analytical assessment of the target molecule, dopamine, at the GCE modified with ERGO.

The initial observation is presented in Fig. 5a, which illustrates the voltammetric curves as the DOP concentration gradually increases from 0.1 μM to 20 μM. The measurements were conducted under optimal conditions in 0.1 M PBS buffer at pH 3.0. The data extracted from these curves reveal that as the DOP concentration increases, the anodic peak current increases proportionally and distinctly. The oxidation peak maintains a sharp morphology and highly stable potentials, demonstrating the robust catalytic activity of the carbon film in accelerating electron-transfer kinetics.

Test conditions: potential scan range −0.2 V–+1.0 V (*vs.* Ag/AgCl), increasing $C_{DOP}$ = 0.1, 0.5, 1.0, 1.5, 2, 7, 13, 20 μM in buffer solution PBS 0.1 M (pH = 3.0), scan rate: 0.2 V $s^{-1}$, pulse amplitude: 0.06 V, rest time: 10 s.

The direct relationship between the peak current and the DOP concentration is clearly illustrated through the analytical calibration plot in Fig. 5b. The recorded data confirm a strong linear dependence across the entire investigated concentration range. The linear regression equation is established as follows:

$$I_{p,\ DOP}\ (\mu A) = (0.496 \pm 0.005) + (1.208 \pm 0.008)C\ (\mu M)$$
$$R = 0.997 \quad (3.8)$$

Based on this calibration model, the LOD ($3\sigma$ formula) for DOP was calculated to be at 0.014 μM.

*For PAR individual determination.* Following the successful quantification of DOP, the individual determination of PAR was thoroughly investigated. Fig. 6a displays the voltammetric profiles recorded as the PAR concentration was systematically increased from 0.1 μM to 20 μM in the same 0.1 M PBS buffer solution at pH 3.0. Similar to the previous observation, the experimental results reveal that the anodic peak current increases proportionally with the analyte concentration.

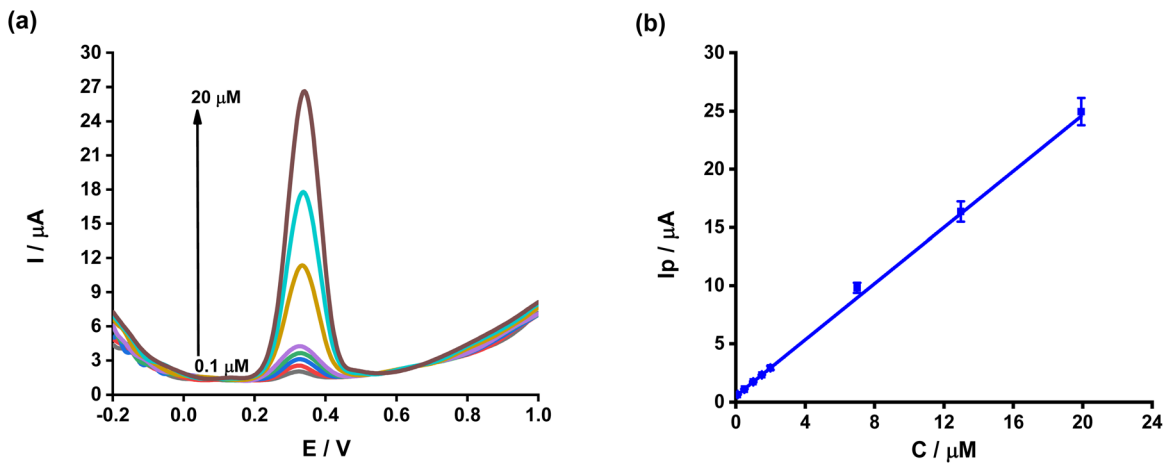


Fig. 5 (a) The DPV curves for the individual determination of DOP at varying concentrations (from 0.1 to 20 μM) employing the ERGO/GCE, and (b) the corresponding analytical calibration plot illustrating the linear dependence of the anodic peak currents on the DOP concentrations.

Test conditions: potential scan range −0.2 V–+1.0 V (*vs.* Ag/AgCl), adding $C_{PAR}$ = 0.1, 0.5, 1.0, 1.5, 2, 7, 13, 20 μM in buffer solution PBS 0.1 M (pH = 3.0), scan rate: 0.2 V $s^{-1}$, pulse amplitude: 0.06 V, rest time: 10 s.

The quantitative relationship is elucidated in Fig. 6b through the corresponding calibration curve. The data exhibit an excellent linear correlation across the tested concentration range. The mathematical model is defined by the following regression equation:

$$I_{p,\ PAR}\ (\mu A) = (0.359 \pm 0.003) + (1.144 \pm 0.002)C\ (\mu M)$$
$$R = 0.999 \quad (3.9)$$

The correlation coefficient value of 0.999 strongly affirms the excellent reliability of this mathematical model. Consequently, the LOD for PAR was determined to be 0.023 μM. These achievements prove that the pure electrochemically reduced film not only broadens the linear dynamic range but also enables the highly precise quantification of both DOP and PAR at ultra-trace levels, thereby satisfying the stringent requirements of pharmaceutical analysis.

**The simultaneous investigation of DOP and PAR.** Building on the excellent quantitative results from individual assessments, the sensing platform's analytical capacity was further challenged by the simultaneous determination of DOP and PAR. This represents the core objective of the research: to definitively resolve the cross-interference issues frequently encountered in complex physiological fluids and in practical pharmaceutical samples.

Fig. 7a presents the DPV curves recorded when the concentrations of both DOP and PAR were simultaneously increased from 0.1 μM to 20 μM. The measurements were conducted in 0.1 M PBS buffer at pH 3.0, with a scan rate of 0.2 V $s^{-1}$. The experimental data illustrate an outstanding catalytic phenomenon where the two oxidation peaks appear completely separated and remarkably sharp. As the concentrations of both analytes elevate, their corresponding anodic peak currents

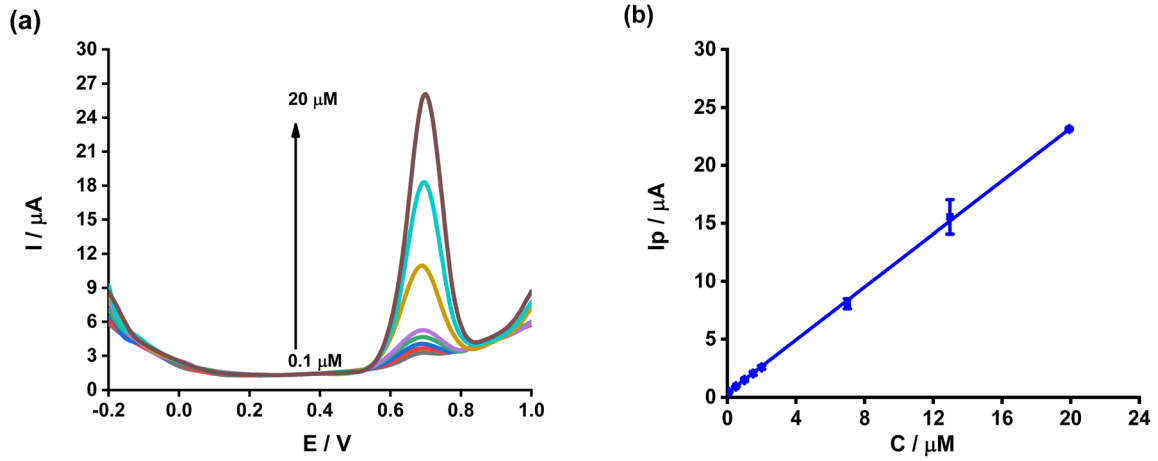


Fig. 6 (a) The DPV curves for the individual determination of PAR at varying concentrations (from 0.1 to 20 μM) employing the ERGO/GCE, and (b) the corresponding analytical calibration plot illustrating the linear dependence of the anodic peak currents on the PAR concentrations.

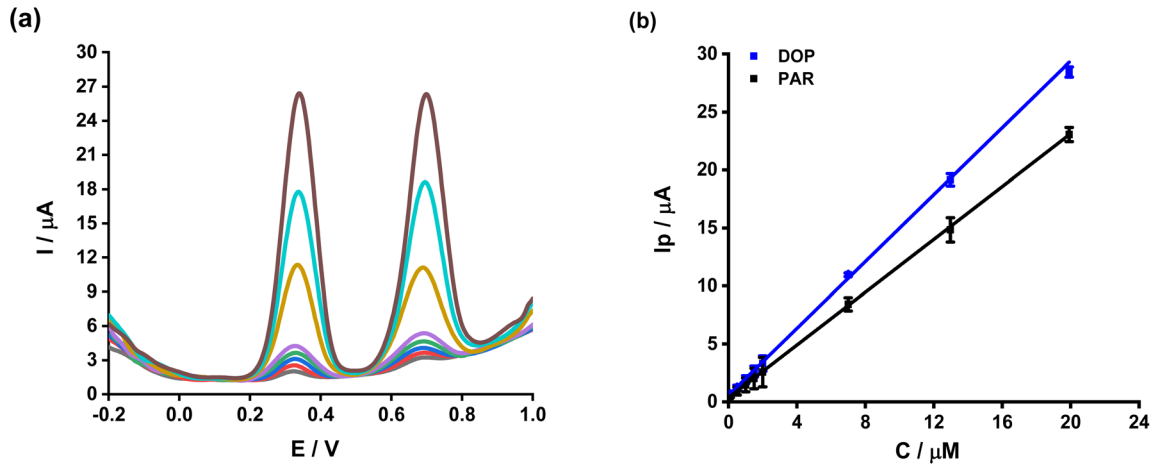


Fig. 7 (a) DPV curves for DOP and PAR at various concentrations applying ERGO/GCE, (b) the linear relationship between $C_{DOP\ and\ PAR}$ *vs.* $I_p$. Test conditions: potential scan range −0.2 V–+1.0 V (*vs.* Ag/AgCl), gradually adding $C_{PAR\ and\ DOP}$ = 0.1, 0.5, 1.0, 1.5, 2, 7, 13, 20 μM in buffer solution PBS 0.1 M (pH = 3.0), scan rate: 0.2 V $s^{-1}$, pulse amplitude: 0.06 V, rest time: 10 s.

Table 1 The comparison performance of detecting DOP and PAR using ERGO and recent reports[a]

| No. | Material | Analyte | Method | LOD (μM) | Linear range (μM) | Real sample | Ref. |
|---|---|---|---|---|---|---|---|
| 1 | H-C/N@$TiO_2$ | DOP | DPV | 0.04 | 0.3–50 | Human serum or saliva | 46 |
| | | PAR | | 0.05 | 0.3–50 | | |
| 2 | 3DRGO/MWNCTs@ZrFeO*x* | DOP | DPV | 0.23 | 1–180 | Real drug and serum samples | 47 |
| | | PAR | | 0.21 | 1–190 | | |
| 3 | CPE-SS | DOP | DPV | 3.6 | 10–1000 | Urine, tap water, pharmaceutical tablets | 48 |
| | | PAR | | 5.54 | 80–1000 | | |
| 4 | RuNPs | DOP | CV | 0.8 | 1–300 | Human blood and | 49 |
| | | PAR | | 0.7 | 1–400 | pharmaceutical formulations | |
| | | DOP | SWV | 0.11 | 1–200 | | |
| | | PAR | | 0.17 | 1–330 | | |
| 5 | BZ-TFP-COF/MWCNTs | DOP | DPV | 0.05 | 0.05–500 | Human blood | 50 |
| | | PAR | | 0.06 | 0.05–500 | | |
| 6 | $NiFe_2O_4$/GP | DOP | CV, DPV | 0.30 | 5–200 | Urine, tablets | 51 |
| | | PAR | | 0.40 | 3–160 | | |
| 7 | CuO/CQDs | DOP | SWV | 25.4 | 180–10 | Pharmaceutical samples and other real samples | 52 |
| 8 | rGO-InZnSe@CeAu-$SiO_2$ QDs | DOP | SWV | 5.0 | 5–1000 | Human serum | 53 |
| 9 | MWCNTs/Pr6O11@W | PAR | CV | 0.0003 | 0.007–1.0 | Pharmaceutical formulations & complex samples | 54 |
| 10 | LSWE | PAR | SW-AdSV | 1.6 | 5–100 | Tablets (pharmaceuticals) | 55 |

[a] H-C/N@$TiO_2$: nitrogen-doped hollow carbon coated with $TiO_2$ double-shelled hollow spheres; 3D RGO/MWCNTs@ZrFeO*x* : ZrFeO*x* nanoparticles anchored on a 3D reduced graphene oxide/multi-walled carbon nanotube network; CPE-SS: shrimp shell waste-modified carbon paste electrode; RuNPs/ASPE: ruthenium nanoparticles modified electrochemically activated screen-printed electrode; BZ-TFP-COF/MWCNTs: benzidine-1,3,5-triformylphloroglucinol covalent organic framework integrated with multi-walled carbon nanotubes; $NiFe_2O_4$/GP: nickel ferrite ($NiFe_2O_4$) modified graphite paste electrode; CQDs/CuO: carbon quantum dots/copper oxide nanocomposite; rGO-InZnSe@CeAu-$SiO_2$ QDs: reduced graphene oxide integrated with InZnSe@CeAu-$SiO_2$ quantum dots; MWCNTs/$Pr_6O_{11}$@W: tungsten-modified praseodymium oxide nanoparticles supported on multi-walled carbon nanotubes; LSWE/PGE: leather shaving waste extract modified pencil graphite electrode.

increase independently without any observable potential shift or peak shape distortion. This observation strongly supports the notion that the carbon nanomaterial provides abundant and independent catalytic centers, enabling the electron–exchange processes of DOP and PAR to occur in parallel without mutual competition or hindrance at the electrode interface.

The quantitative relationship during the simultaneous analysis is elucidated in detail through the calibration plots in Fig. 7b. Similar to the individual determinations, the catalytic peak current shows a linear dependence on the concentration of each analyte across the entire investigated range. Linear regression analysis generated the following precise mathematical models:

$$I_{p,DOP}\ (\mu A) = (0.349 \pm 0.014) + (1.139 \pm 0.004)C_{DOP}\ (\mu M)$$
$$R = 0.999 \quad (3.10)$$

$$I_{p,\ PAR}\ (\mu A) = (0.571 \pm 0.109) + (1.442 \pm 0.020)C_{PAR}\ (\mu M)$$
$$R = 0.999 \quad (3.11)$$

The correlation coefficient value reaches an exceptional 0.999 for both models, proving the absolute reliability of the sensing platform in a multicomponent environment. Based on these standard calibration equations, the LOD was calculated to achieve highly impressive levels of 0.008 μM for DOP and 0.016 μM for PAR. Notably, the LOD obtained during the simultaneous measurements is even lower than that from the individual assessments, suggesting a highly positive synergistic catalytic effect on the surface of the electrochemically reduced film.

To underscore the scientific value of this research, the analytical performance of the proposed sensing platform was systematically compared with that of recently published advanced modified electrodes, as comprehensively summarized in Table 1. It is clearly evident that the GCE modified with the green-synthesized nanomaterial exhibits superior performance. This platform not only achieves LOD at ultra-trace levels but also maintains a broad linear dynamic range, directly competing with highly complex architectures, such as precious-metal nanoparticles or molecularly imprinted polymer networks. This remarkable achievement convincingly demonstrates that the simple, reagent-free electrode fabrication process is fully capable of creating an exceptionally powerful analytical tool that excellently meets the stringent standards for the simultaneous monitoring of pharmaceutical compounds.

## Interferents

Following the successful achievement of the ultra-low LOD and a broad linear dynamic range, it is essential to evaluate the analytical selectivity of the proposed sensor. This evaluation serves as a critical bridge between ideal laboratory conditions and the highly complex environments found in actual physiological fluids and pharmaceutical matrices.

Table 2 meticulously summarizes the impact of various common inorganic ions and coexisting biological molecules on

Table 2 The influence of various potential interfering species on the simultaneous electrochemical detection of dopamine and paracetamol

| Interferents | Interferents : DOP ratio | RE (%) | Interferents : PAR ratio | RE (%) |
|---|---|---|---|---|
| $(NH_4)_2SO_4$ | 80 | 4.2 | 100 | −3.1 |
| NaCl | 90 | −1.5 | 90 | 0.8 |
| $FeCl_3$ | 100 | 3.7 | 70 | 2.4 |
| $Ca(NO_3)_2$ | 50 | 4.8 | 80 | −1.9 |
| Uric acid | 80 | −0.4 | 100 | −1.2 |
| Hypoxanthine | 100 | 1.1 | 80 | −2.6 |
| Clenbuterol | 150 | −3.2 | 120 | 4.5 |
| Ascorbic acid | 100 | 2.8 | 150 | −0.7 |

the simultaneous oxidation signals of DOP and PAR. Acceptance was defined *a priori* as a RE within ±5%. To rigorously challenge the sensing interface, these potential interferents were deliberately introduced into the analytical solution at concentrations up to 150 times those of the target analytes.

The experimental data clearly show that high concentrations of inorganic salts, including ammonium sulfate, sodium chloride, iron chloride, and calcium nitrate, induced negligible fluctuations in the catalytic peak currents. The calculated RE values consistently remained well within the acceptable analytical threshold of 5%.

More importantly, the sensor demonstrated exceptional resistance to highly electroactive biological compounds, including ascorbic acid, uric acid, and hypoxanthine. On conventional, unmodified carbon surfaces, these specific molecules typically undergo oxidation at proximate potentials, leading to severe signal overlap and false-positive readings. However, on the ERGO platform, a 100-fold excess of ascorbic acid resulted in a mere 2.8% RE for DOP, while a 150-fold excess generated only a negative 0.7% error for PAR. Similarly, organic compounds such as clenbuterol caused minimal current deviation even at 150- and 120-fold excesses relative to DOP and PAR, respectively.

Concurrently, the precisely tuned pH 3.0 operating environment effectively suppresses the electrochemical activity of the interfering species at the specific oxidation potentials of the target molecules. By successfully overcoming the critical hurdle of biological interference, these results complete the sensor's analytical profile. The data clearly demonstrate the exceptional robustness of the electrocatalytic interface, confirming that this sensing platform is well-suited for highly accurate real-world diagnostic applications.

## Repeatability and reproducibility

To critically evaluate the practical viability of the engineered sensing platform, its operational stability was rigorously tested through repeatability and reproducibility assessments. These parameters are absolutely essential to confirm that the electrocatalytic interface does not suffer from rapid passivation and that the completely reagent-free fabrication process is highly consistent.

**Repeatability**

The repeatability of the analytical signal was evaluated by recording six consecutive DPV curves for the simultaneous detection of DOP and PAR. To ensure a comprehensive evaluation, this consecutive testing was conducted systematically at three distinct concentration levels: 0.1 μM, 1.0 μM, and 20 μM, corresponding to Fig. 8a–c, respectively.

The experimental data yielded highly stable current responses across all consecutive trials. Specifically, the RSD values for DOP were calculated to be 4.9%, 4.1%, and 3.7% for the respective increasing concentrations. Concurrently, the RSD values for PAR were determined to be 5.0%, 4.2%, and 3.5%, respectively. To further validate the scientific rigor of these results, the experimental deviations were rigorously compared with the Horwitz standard limits. Because DOP and PAR have approximately the same molecular mass, the accepted $\frac{1}{2}RSD_{Horwitz}$ values ($RSD_{Horwitz} = 2^{1-0.5\log C}$, where $C$ is the fraction concentration of the analysis compound)[56] at 0.1 μM, 1.0 μM, and 20 μM are 22.6%, 16.0%, and 10.5%, respectively.[57] It is clear that all the experimental deviations obtained from the sensor are far below these maximum allowable limits. This outstanding repeatability definitively proves that the pristine two-dimensional carbon film effectively resists the strong adsorption of oxidized pharmaceutical byproducts.[57] This remarkable anti-fouling capability ensures the continuous analytical reliability of the sensor even after multiple measurement cycles.

## Reproducibility

In addition to the operational stability of a single run, the fabrication consistency of the green synthesis method was thoroughly investigated. Fig. 9 presents the voltammetric responses for the simultaneous detection of DOP and PAR at a fixed concentration of 1.0 μM, utilizing five successive modifications on a single GCE.

The recorded catalytic peak currents displayed excellent uniformity across all five independent fabrication cycles. The statistical analysis yielded impressively low RSD of 2.7% for DOP and 3.1% for PAR. This minimal variance convincingly demonstrates that the direct electrochemical reduction technique provides precise control over both the deposition rate and the degree of structural reduction. Consequently, this sustainable approach ensures highly reproducible generation of a uniform, defect-rich catalytic interface, making the proposed platform exceptionally well-suited for routine clinical and pharmaceutical monitoring.

## The real sample analysis

To definitively validate the practical applicability and clinical relevance of the engineered sensing platform, the proposed electrode was utilized to quantify DOP and PAR in actual commercial pharmaceutical formulations. This crucial final step bridges the gap between controlled laboratory testing and highly complex real-world diagnostic applications.

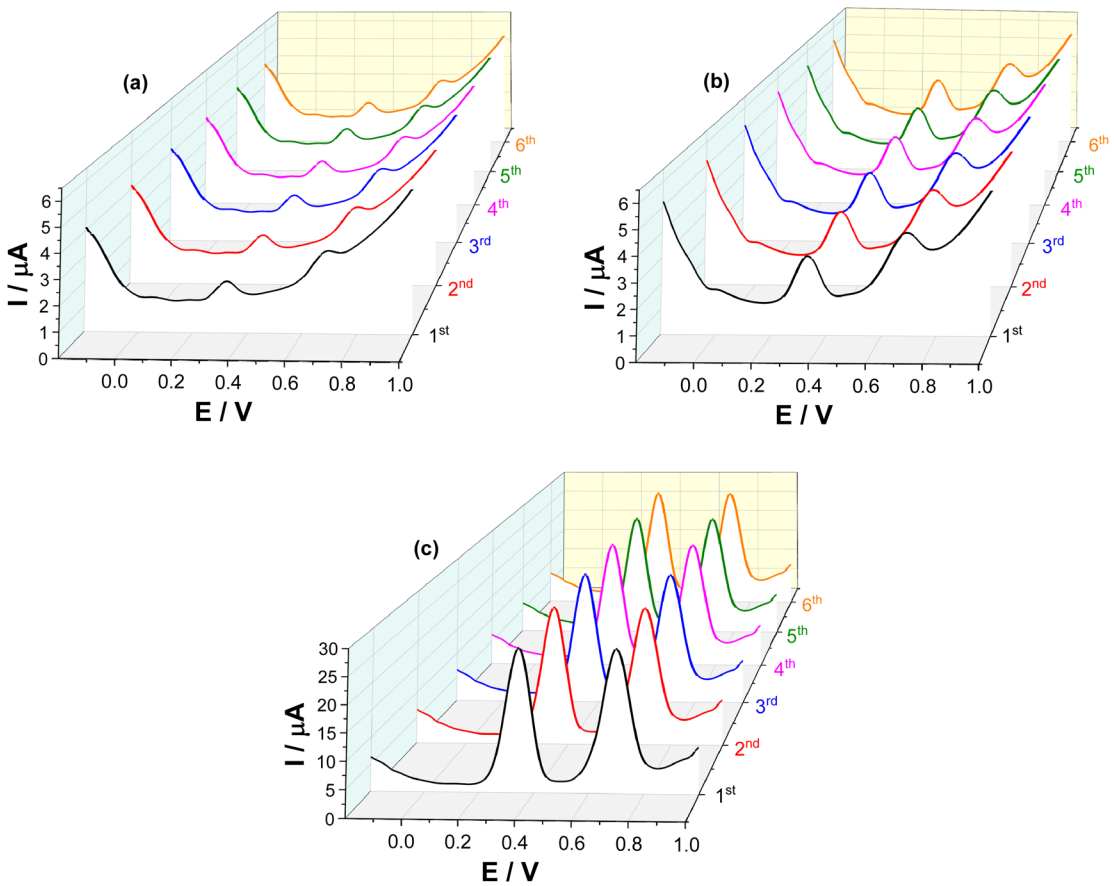


Fig. 8 DPVs for DOP and PAR at 3 different concentrations: (a) 0.1 μM, (b) 1.0 μM, (c) 20 μM. Test conditions: potential scan range −0.2 V–+1.0 V (*vs.* Ag/AgCl), scan rate: 0.2 V $s^{-1}$, pulse amplitude: 0.06 V, rest time: 10 s.

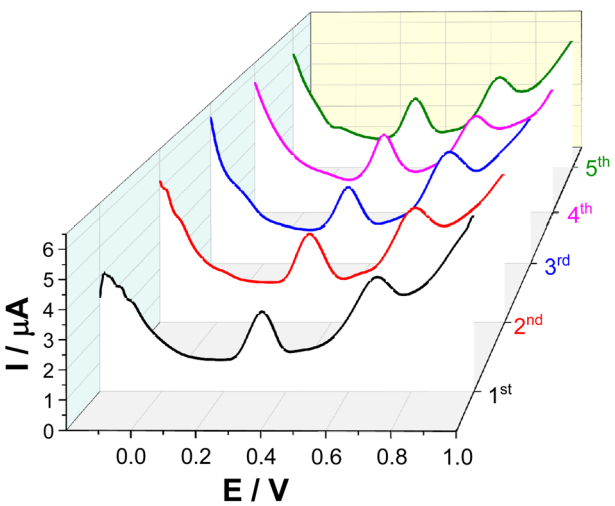


Fig. 9 The DPVs for DOP and PAR at 1.0 μM, with five successive modifications on a single GCE. Test conditions: potential scan range −0.2 V–+1.0 V (*vs.* Ag/AgCl), scan rate: 0.2 V $s^{-1}$, pulse amplitude: 0.06 V, rest time: 10 s.

The analytical accuracy was evaluated using the standard-addition method with six different commercial medications. The DPV measurements yielded highly impressive results, with excellent recovery rates of 96.1% to 104.1%. These optimal recovery values clearly indicate that the complex matrix components and various excipients inherently present in these commercial formulations did not interfere with the electrocatalytic signals of the target analytes.

To further confirm the absolute reliability and precision of the ERGO sensor, the results obtained with the proposed method were rigorously compared with those from the gold-standard HPLC technique. A comprehensive statistical evaluation confirmed that there is no significant difference between the two analytical methodologies. For the quantification of DOP, $t(5) = 0.73$, $p$-value $= 0.50$. Similarly, the statistical analysis for PAR yielded $t(5) = 0.48$, $p$-value $= 0.65$. Because both $p$-values are substantially greater than the standard 0.05 significance threshold, it is statistically proven that the developed electrochemical sensor provides an equivalent level of accuracy to the highly sophisticated and expensive chromatographic instrument (Table 3).

By successfully quantifying the target pharmaceutical molecules in complex commercial matrices with exceptional precision, these results seamlessly complete the scientific narrative of this study. The completely reagent-free fabrication process yields an advanced electrocatalytic interface that is not only ultra-sensitive and highly selective but also perfectly capable of

Table 3 The quantitative analysis of DOP and PAR in real pharmaceutical samples utilizing the proposed DPV method and the standard HPLC method[a]

| | | DPV | | | | HPLC | |
|---|---|---|---|---|---|---|---|
| Medication | Analyte | $C_I$ (μM) | $C_A$ (μM) | $C_F$ (μM) | Rev (%) | $C_I$ (μM) | $C_F$ (μM) |
| Panadol extra | PAR | 50.25 | 50 | 98.62 | 96.7 | 50.8 | 98.77 |
| Efferalgan | PAR | 49.82 | 50 | 99.15 | 98.7 | 49.55 | 99.05 |
| Hapacol 150 | PAR | 19.45 | 50 | 71.34 | 103.8 | 19.77 | 71.24 |
| Dopamin–Giulini | DOP | 9.72 | 10 | 20.12 | 104.0 | 10.12 | 19.77 |
| Limdopa Inj. 200 mg | DOP | 10.18 | 10 | 19.79 | 96.1 | 9.74 | 20.09 |
| Dopamin–Rotexmedica | DOP | 9.91 | 10 | 20.32 | 104.1 | 10.02 | 19.83 |

[a] $C_I$ = initial concentration, $C_A$ = added concentration, $C_F$ =found concentration.

serving as a robust, cost-efficient, and rapid analytical tool for routine pharmaceutical quality control and clinical monitoring.

## Conclusions

An advanced sensing platform for the simultaneous determination of dopamine and paracetamol was successfully constructed utilising a sustainable methodology. The critical challenges of signal convolution and surface fouling were effectively overcome by the direct electrodeposition of reduced graphene oxide. By employing this green synthesis strategy, the electrical conductivity of the two-dimensional carbon lattice was restored without introducing toxic impurities. Consequently, a pristine boundary was established, facilitating accelerated electron transfer and enabling complete baseline separation of the target molecules. Quantitatively, the analytical capability of the modified electrode was demonstrated by a broad linear dynamic range from 0.1 to 20 μM and ultratrace limits of detection of 0.008 μM and 0.016 μM for dopamine and paracetamol, respectively, alongside strong resistance to common biological interferents. The clinical applicability of the method was ultimately confirmed by the successful quantification of both analytes in complex commercial medications, and the analytical accuracy was validated against sophisticated chromatographic techniques. Ultimately, this research delivers a robust, cost-efficient, and environmentally friendly analytical tool that offers significant scientific value for future point-of-care diagnostics and routine pharmacological screening.

## Conflicts of interest

The authors declare no conflict of interest.

## Data availability

All data supporting this study are available within the article.

## Acknowledgements

This research was funded by University of Medicine and Pharmacy, Hue University, under grant number 08/26.

## References

1 R. I. Teleanu, A.-G. Niculescu, E. Roza, O. Vladâcenco, A. M. Grumezescu and D. M. Teleanu, *Int. J. Mol. Sci.*, 2022, **23**, 5954.
2 L. Speranza, M. C. Miniaci and F. Volpicelli, *Biomedicines*, 2025, **13**(2), 492.
3 S. A. Factor, D. Weinshenker and J. L. McKay, *J. Parkinson's Dis.*, 2025, **15**(2), 282–290.
4 J. A. Johnson and R. M. Wightman, *Electrochem. Soc. Interface*, 2017, **26**, 53–57.
5 E. S. Bucher and R. M. Wightman, *Annu. Rev. Anal. Chem.*, 2015, **8**, 239–261.
6 S. Alwarappan, K. S. A. Butcher and D. K. Y. Wong, *Sensor. Actuator. B Chem.*, 2007, **128**, 299–305.
7 S. Alwarappan, G. Liu and C.-Z. Li, *Nanomed. Nanotechnol. Biol. Med.*, 2010, **6**, 52–57.
8 S. Alwarappan, A. Erdem, C. Liu and C.-Z. Li, *J. Phys. Chem. C*, 2009, **113**, 8853–8857.
9 N. O. Gomes and P. A. Raymundo-Pereira, *Small*, 2023, **19**, 2206753.
10 G. Shams and S. Elmesiry, *Zag. Vet. J.*, 2022, **50**, 219–227.
11 B. Patella, A. Sortino, F. Mazzara, G. Aiello, G. Drago, C. Torino, A. Vilasi, A. O'Riordan and R. Inguanta, *Anal. Chim. Acta*, 2021, **1187**, 339124.
12 D. Chen, J.-X. Zhang, W.-Q. Cui, J.-W. Zhang, D.-Q. Wu, X.-R. Yu, Y.-B. Luo, X.-Y. Jiang, F.-P. Zhu and D. Hussain, *J. Chromatogr., A*, 2021, **1654**, 462474.
13 J. Wang, *Chem. Rev.*, 2008, **108**, 814–825.
14 M. H. Rahman, M. A. Rashed, N. I. Nayem, M. A. Rahaman, J. Ahmed, M. Faisal, M. Jalalah and F. A. Harraz, *Mater. Chem. Phys.*, 2024, **314**, 128915.
15 N. An, N. Su, X.-R. Li, J.-Y. Liu and Q.-Y. Wang, *J. Electrochem.*, 2025, **31**, 3.
16 A. Ali, S. M. Majhi, L. A. Siddig, A. H. Deshmukh, H. Wen, N. N. Qamhieh, Y. E. Greish and S. T. Mahmoud, *Biosensors*, 2024, **14**, 497.
17 X. Li, G. Wu, C. Pan and R. Bao, *J. Semicond.*, 2025, **46**, 11607.
18 D. Coban, Y. Tangal and S. Cogal, *J. Mater. Sci.: Mater. Electron.*, 2024, **35**, 1513.

 

19 N. O. Gomes, S. C. Teixeira, M. L. Calegaro, S. A. S. Machado, N. de F. F. Soares, T. V. de Oliveira and P. A. Raymundo-Pereira, *Chem. Eng. J.*, 2023, **472**, 144775.
20 E. N. M. Mahbob, M. S. Ahmad, I. M. Isa, N. Hashim and A. Ul, *J. Chem. Soc. Pak.*, 2024, **46**, 130–145.
21 A. K. Geim and K. S. Novoselov, *Nat. Mater.*, 2007, **6**, 183–191.
22 A. Parihar, K. Nambiar, S. Pawar and R. Khan, *Biosens. Bioelectron.:X*, 2026, 100737.
23 A. Parihar, P. Vishwakarma and P. Prajapati, *Biosens. Bioelectron.*, 2025, **268**, 116925.
24 S. Bose, T. Kuila, M. E. Uddin, N. H. Kim, A. K. T. Lau and J. H. Lee, *Polymer*, 2010, **51**, 5921–5928.
25 L. Hou, J. Wei, C. Xiang, D. Yang and Y. Yang, *Microchim. Acta*, 2025, **192**, 1–12.
26 K. Guzelaydin, Y. Gunes, C. Anlas and M. Yildirim, *J. Vet. Sci.*, 2025, **26**, e21.
27 J. Wang, X. Li, R. Peng, J. Dong, J. Zhang, Z. Lu, X. Zhu, J. Zhang, Y. Mao and X. Liu, *Chem. Eng. J.*, 2025, 160066.
28 A. Becze, M.-A. Resz, A. Ilea and O. Cadar, *Appl. Sci.*, 2022, **12**, 9789.
29 V. Menaka and D. Geetha, *Ionics*, 2025, 1–17.
30 N. S. Md Rudin, M. A. I. Mohd Yassin and M. F. Omar, *Fullerenes, Nanotubes, Carbon Nanostruct.*, 2025, 1–9.
31 A. Y. Liu and M. L. Cohen, *Science*, 1989, **245**, 841–842.
32 R. Sharma, G. Lakshmi, A. Kumar and P. Solanki, *ECS Sens. Plus*, 2022, **1**, 10603.
33 D. L. Glasco, A. Sheelam, N. H. B. Ho, A. M. Mamaril, M. King and J. G. Bell, *ECS Sens. Plus*, 2022, **1**, 010602.
34 V. Chaudhary, A. K. Kaushik, H. Furukawa and A. Khosla, *ECS Sens. Plus*, 2022, **1**, 013601.
35 A. Khosla, *ECS Sens. Plus*, 2022, **1**, 10001.
36 T. L. Andrew, S. Rostaminia, S. Z. Homayounfar and D. Ganesan, *ECS Sens. Plus*, 2022, **1**, 11602.
37 N. H. B. Ho, D. L. Glasco and J. G. Bell, *ECS Sens. Plus*, 2022, **1**, 20601.
38 A. Ahad and M. Tahir, *ECS Sens. Plus*, 2023, **2**, 11601.
39 H. C. A. Murthy, K. G. Kelele, C. R. Ravikumar, H. P. Nagaswarupa, A. Tadesse and T. Desalegn, *Results Chem.*, 2021, **3**, 100131.
40 E. T. Mombeshora and E. Muchuweni, *RSC Adv.*, 2023, **13**, 17633–17655.
41 Y. Zhang, *Alexandria Eng. J.*, 2024, **96**, 185–194.
42 A. R. Marlinda, S. Sagadevan, N. Yusoff, A. Pandikumar, N. M. Huang, O. Akbarzadeh and M. R. Johan, *J. Alloys Compd.*, 2020, **847**, 156552.
43 B. Dey, M. W. Ahmad, G. Sarkhel, G. Ho Lee and A. Choudhury, *Microchem. J.*, 2023, **186**, 108295.
44 E. J. Laviron, *J. Electroanal. Chem. Interfacial Electrochem.*, 1979, **101**, 19–28.
45 E. Methodology.
46 H. Yang, G. Cao, Y. Huang, Y. Lin, F. Zheng, L. Lin, F. Liu and S. Li, *J. Pharm. Anal.*, 2022, **12**, 436–445.
47 A. Xie, H. Wang, J. Lin, J. Pan, M. Li, J. Wang, S. Jiang and S. Luo, *J. Alloys Compd.*, 2023, **938**, 168647.
48 M. Achache, G. Elouilali Idrissi, N. Ben Seddik, S. El Boumlasy, I. Kouda, I. Raissouni, F. Chaouket, K. Draoui, D. Bouchta and M. Choukairi, *Microchem. J.*, 2024, **202**, 110754.
49 D. Ghediri, R. Kihal, M. L. Chelaghmia, A. K. Assaifan, C. E. Banks, F. Z. Makhlouf, H. Fisli, M. Nacef, A. M. Affoune, S. M. Foukmeniok and M. Pontié, *Microchem. J.*, 2025, **215**, 114186.
50 R. Younas, I. Naz, A. Tariq, M. B. K. Niazi and F. Jubeen, *Electrochim. Acta*, 2025, **539**, 147165.
51 Y. Kumar, S. Sharma, K. B. Mishra, M. V. Singh, V. R. Pullabhotla and P. Pramanik, *J. Indian Chem. Soc.*, 2025, **102**, 101633.
52 S. E. Elugoke, O. E. Fayemi, A. S. Adekunle, B. B. Mamba, T. T. I. Nkambule and E. E. Ebenso, *FlatChem*, 2022, **33**, 100372.
53 K. I. Gray, S. Zolotovskaya and O. Adegoke, *Microchem. J.*, 2026, **220**, 116664.
54 E. Beyyavaş and M. Aslanoglu, *Surf. Interfaces*, 2026, **86**, 108779.
55 W. Bosnali, Ş. Korkmaz, A. D. Mülazımoğlu and İ. E. Mülazımoğlu, *ACS Omega*, 2025, **10**(18), 18270–18282.
56 W. Horwitz and R. Albert, *Analyst*, 1997, **122**, 615–617.
57 P. R. Dalmasso, M. L. Pedano and G. A. Rivas, *Sens. Actuators, B*, 2012, **173**, 732–736.